Revision 3

Vergasovaite to cupromolybdite topotactic transformation with crystal shape preservation

Evgeni V. Nazarchuk[1], Oleg I. Siidra[1,2*], Dmitri O. Charkin[3], Gleb V. Nikolaevich[3], Artem S. Borisov[1], and Valery L. Ugolkov[4]

[1]Department of Crystallography, Saint-Petersburg State University, University emb. 7/9, St. Petersburg 199034 Russia

[2]Kola Science Center, Russian Academy of Sciences, Apatity, Murmansk Region, 184200 Russia

[3]Department of Chemistry, Moscow State University, Vorobievy Gory 1, bd. 3, Moscow 119991 Russia

[4]Institute of Silicate Chemistry, Russian Academy of Sciences, Adm. Makarova emb. 2, 199034 St. Petersburg, Russia

E-mail: o.siidra@spbu.ru

Abstract

Thermal behavior of vergasovaite, ideally $Cu_3O(SO_4)(MoO_4)$, and its synthetic analogue has been studied by high-temperature single crystal X-ray diffraction in the temperature range of 300-1100 K. According to the EMPA results, the empirical formulas are $(Cu_{2.36}Zn_{0.61})_{\sum=2.97}O[(Mo_{0.91}S_{0.08}V_{0.04})_{\sum=1.03}O_4](SO_4)$ for vergasovaite and $Cu_{2.97}O[(Mo_{0.92}S_{0.09})_{\sum=1.01}O_4](SO_4)$ for its synthetic analogue. The mineral is stable until 950±15 K; at 975 K, the unit-cell parameters and volume increase abruptly due to topotactic transformation of vergasovaite into cupromolybdite, $Cu_3O(MoO_4)_2$. The transformation is accompanied by loss of sulfur (and excess copper) without destruction of the crystal. The thermal expansion of the vergasovaite structure is strongly anisotropic, being minimal along the $[O_2Cu_6]^{8+}$ chains comprised of vertex-sharing OCu_4 tetrahedra. The peculiarities of the thermal expansion of vergasovaite can be explained by the anisotropy of bond length evolution in the $Cu1O_6$ and $Cu3O_6$ octahedra and flexibility of the S-O-Cu and Mo-O-Cu bond angles. Synthetic Zn- and V-free analogue demonstrates negative thermal expansion at 425-625 K and melts at as low temperature as 700 K with no indication of transformation or recrystallization at least below 1200 K.

The topotactic transformation observed for copper sulfate molybdate, vergasovaite may bring new ideas and become an exciting playground for the preparation of self-regenerating compounds with such magnetic ions as Cu^{2+}.

Keywords: Topotactic transformations; Sulfates; Molybdates; Fumarolic minerals; Vergasovaite; Single crystal X-ray diffraction; Thermal expansion

1. Introduction

The recent progress in X-ray diffraction techniques and software has accelerated in-situ studies of single crystals under non-ambient conditions. The practical importance of studying such phenomena can hardly be overestimated. Single-crystal-to-single-crystal (SC-SC) transformations have attracted great attention due to the excellent opportunity to study structure-property relationships for different materials in addition to other methods (Sahoo et al. 2011; Müller et al. 2015). However, the overhelming majority of reports are devoted to SC-SC transformations in organic or metal-organic compounds, whereas there are only few papers on these phenomena occurring in purely inorganic (Peryshkov et al. 2010; Kahlenberg et al. 2015) and especially anhydrous (Iordanidis and Kanatzidis, 2000; Wang et al. 1998) systems, wherein the SC-SC transitions are exceptionally rare, since single-crystal integrity is generally destroyed during the phase transformation process. An example of "successful" transition is $Ln_2[(UO_2)_2V_2O_8]_3 \cdot nH_2O$ series (Mer et al. 2019): upon heating, these crystals can transform from water-rich (n = 28) to water-poor (n = 6) hydrates, and despite the very essential volume shrinkage (ΔV = -27.8%), the crystal retains enough perfectness for structural studies; the (de)hydration is fully reversible. Topotactic transitions in single crystals were described for a number of minerals and inorganic compounds (Dent-Glasser et al. 1962; Nicol 1963; Fei et al. 2012). For example, the recent studies of dumortierite-like compounds (Mentré et al. 2018) revealed an oxidative exsolution of a part of iron at the crystal surface in the form of hematite and amorphous Fe phases during heating experiments. Metal catalyst formation as a result of the segregation from oxide crystal lattice during exsolution processes became of a great interest in materials science (Neagu et al. 2013). Kinetics of these processes is very fast and usually very difficult to register and study for the understanding of underlying mechanisms. Control of such transformations is crucial because many materials undergo solid-solid transitions between various forms as a function of temperature or pressure.

The copper sulfate-oxides and molybdate-oxides are of essential interest from geological, physical, and chemical aspects. Studies of these minerals may help in better understanding of the

geochemistry and mineralogy of the oxidation areas of molybdenum deposits and evolution of mineral parageneses of the active fumaroles with strongly oxidizing environments. For instance, the nearly forty-year mineralogical investigations of the slag cones of the Tolbachik volcano on Kamchatka peninsula (Vergasova and Filatov 1993, 2016) revealed as many as 350 mineral species, a type locality for at least 123 (Pekov et al. 2020). The highest diversity of exhalative mineral species is observed for the fumaroles of the Second Scoria Cone (SSC hereafter) of the Great Tolbachik Fissure Eruption (1975–1976, GTFE hereafter) and likewise in the Naboko scoria cone of the 2012–2013 Tolbachik Fissure eruption (FTE). A number of GTFE minerals are now being considered as archetypes for unique magnetic materials (Botana et al. 2018; Fujihala et al. 2017; Bartrutdinov et al. 2018; Siidra et al., 2020, Nekrasova et al., 2021).

Despite the large number of sulfate minerals (e.g. Siidra et al. 2017) discovered in GTFE fumaroles, there is just a handful of molybdate species unambiguously detected including cupromolybdite $Cu_3O(MoO_4)_2$ (Zelenski et al. 2012), and vergasovaite $Cu_3O(SO_4)(MoO_4)$ (Bykova et al. 1998). Vergasovaite has been discovered in 1999 among the exhalations of the Yadovitaya (Poisonous) fumarole in association with some other rare copper-sulfate species. This mineral is isostructural to $Cu_3O(MoO_4)_2$ (Berlepsch et al. 1999) first synthesized in 1956 by annealing together MoO_3 and CuO (Thomas et al. 1956). Crystals of $Cu_3O(MoO_4)_2$ can be prepared by heating lindgrenite $Cu_3(MoO_4)_2(OH)_2$ in air stream at 643 – 683 K (Vilminot et al. 2009), at 973-1023 K via chemical transport using Br_2 (Steiner et al. 1996); and hydrothermal synthesis which, under certain conditions, leads to a different polymorph (Hara and Sato 2013). Vergasovaite, ideally $Cu_3O(SO_4)(MoO_4)$, exhibits an ordered version of the cupromolybdite structure with *T*1 site jointly occupied by Mo, S and minor V, the other *T*2 site being fully occupied by sulfate (Berlepsch et al., 1999). Such ordering may stem from both size and chemical differences, as exemplified by some more GTFE minerals with ordering of different tetrahedral anions (e.g. aleutite $(Cu_5O_2)(AsO_4)(VO_4)\cdot(Cu_{0.5}\square_{0.5})Cl$ (Siidra et al. 2019) and vasilseverginite $Cu_9O_4(AsO_4)_2(SO_4)_2$ (Pekov et al. 2021)). Synthetic analogues of vergasovaite have not been reported to date.

Over the past decades, high-temperature X-ray studies have been performed for many hydrated sulfate mineral species (e.g. Ballirano et al. 2015; Balić-Žunić et al. 2016), while anhydrous sulfates are much less studied. The overall goal of our research has been to determine thermal behavior including thermal expansion of various anhydrous sulfate mineral species of fumarolic origin. To do so, we have studied kamchatkite, chalcocyanite, euchlorine, dolerophanite and vergasovaite. Hereby we report the results of variable-temperature (300-1150 K) single-crystal X-ray studies of vergasovaite as well as its synthetic analog whose behavior at high temperatures turned out to be unprecedented and deserves a detailed study.

2. Materials and methods

2.1 Mineral occurrence

The crystals were collected by the authors at the Yadovitaya (Russian for Poisonous) fumarole, SSC, GTFE. Samples of vergasovaite (Fig. 1) used in the study were recovered from 1.5 m depth. The temperature of the gases at the sampling location was approximately 350 °C. Immediately after recovery, the samples were sealed off on-site and thus isolated from the humid atmosphere. Vergasovaite forms single crystals up to 1-2 mm long deposited directly from volcanic gas emissions as a sublimate. In the selected samples, it associates mainly with chalcocyanite $CuSO_4$, kamchatkite $KCu_3O(SO_4)_2Cl$, alumoklyuchevskite $K_3Cu_3O_2(Al,Fe^{3+})(SO_4)_4$, euchlorine $KNaCu_3O(SO_4)_3$, anhydrite $CaSO_4$ and langbeinite $K_2Mg_2(SO_4)_3$. Several cases have been reported when vergasovaite associates with cupromolybdite $Cu_3O(MoO_4)_2$ (Zelenski et al., 2012).

2.2 Synthesis of vergasovaite analogue

The synthetic approach was targeted at single crystal growth and attempted to emulate the natural conditions of cupromolybdite/vergasovaite formation in active fumaroles. Mixtures of K_2SO_4 (added for lowering the melting point), $CuSO_4 \cdot 5H_2O$, CuO and MoO_3 in (1-2):2:(2-3):1 ratio with overall sample mass of ~5 g were placed in porcelain boats inside an open silica tube (inner diameter 20–25 mm) which were placed into a horizontal furnace. A stream of air (0.5–0.7 l/min) was passed through a wash bottle containing 50 ml of concentrated (37%, *ca*. 9.3 mol/l) hydrochloric acid and directed into the tube imitating the fumarolic gas stream. The samples (one sample for a single experiment) were heated to 1040 K in 2 hrs, soaked at this temperature for the same time, after which the tube was stoppered and taken rapidly out of the furnace. The black viscous melt solidified in approximately 10 minutes; the boat was taken out of the tube after cooling to room temperature. Brown needles of copper molybdates and green acicular crystals of synthetic vergasovaite (Fig. 1) were formed. The boats were kept in tightly closed polypropylene vials prior to analysis.

2.3 Chemical composition

Selected crystals of vergasovaite and its synthetic analogue were embedded into epoxy resin, polished and coated with carbon film. Electron microprobe analyses (EMPA) were carried out in energy dispersive mode (acceleration voltage 20 kV, beam current 2 nA, acquisition time 30 s per point), by means of a Hitachi S-3400N scanning electron microscope equipped with an Oxford Instruments X-Max 20 spectrometer, and interpreted using the *Oxford AzTec* software package. The following analytical standards were used: $CaSO_4$ (S*K*α), metallic Cu (Cu*K*α), Mo (Mo*L*α), Zn (Zn*K*α) and V (V*K*α). Other elements were found below the detection limits.

This is the peer-reviewed, final accepted version for American Mineralogist, published by the Mineralogical Society of America.
The published version is subject to change. Cite as Authors (Year) Title. American Mineralogist, in press.
DOI: https://doi.org/10.2138/am-2022-8753. http://www.minsocam.org/

According to the EMPA results (Table 1), the empirical formulas are $(Cu_{2.36}Zn_{0.61})_{\sum=2.97}O[(Mo_{0.91}S_{0.08}V_{0.04})_{\sum=1.03}O_4](SO_4)$ for vergasovaite and $Cu_{2.97}O[(Mo_{0.92}S_{0.09})_{\sum=1.01}O_4](SO_4)$ for its synthetic analogue.

Table 1. Chemical composition of studied vergasovaite and its synthetic analogue.

	Mineral*		Synthetic**		Formula amounts***		
	Wt%	Range	Wt%	Range	Cation	Natural	Synthetic
SO_3	18.97	17.88–20.40	19.08	17.91–20.09	S	1.08	1.09
MoO_3	28.80	27.78–30.12	29.15	28.02–30.23	Mo	0.91	0.92
V_2O_5	0.74	0.21–1.58			V	0.04	
CuO	41.47	40.63–42.06	51.80	50.97–52.32	Cu	2.36	2.97
ZnO	10.97	10.00–11.29			Zn	0.61	
Total	100.95		100.04				

*Average of nine analyses
**Average of five analyses
***Calculated based on nine oxygen atoms per formula unit

2.4 Thermal analysis

The experiments were conducted on a STA 429 CD NETZSCH device equipped with a Pt/PtRh sample holder of the «TG + DSC» type and a quadrupole QMS 403 C NETZSCH mass spectrometer. Polycrystalline NM sample was placed in a fused alumina crucible with a cover with an aperture in the centre. After weighing ±0.01 mg, the crucible was mounted on the holder and subject to complex thermal analysis with a heating ramp of 20 K/min in air flow (50 cm^3/min) in the temperature range of the 300 – 1400 K. Mass losses (mg) and enthalpy changes (mW/mg) were registered simultaneously (Fig. S1).

Between 950 and 1100 K, the differential scanning calorimetry (DSC) curve for ***VM*** exhibits an endothermic effect with a maximum at 1008 K, which corresponds to the step in the thermal gravimetry (TG) curve. Upon further heating between 1100 and 1400 K, the DSC curve exhibits a deflection into endothermal region. The peak at 1322 K corresponds to the chemical decomposition of the ***VM*** sample.

The DSC curve of ***SA*** exhibits an endothermal effect culminating at 698 K, which most likely corresponds to its decomposition.

2.5 Single-crystal X-ray experiment

Single-crystal X-ray data of vergasovaite and synthetic analogs (Table 2) were collected using a Rigaku XtaLAB Synergy-S diffractometer equipped with a PhotonJet-S detector operating with MoKα radiation at 50 kV and 1 mA. Crystals with dimensions of 0.15×0.11×0.12 mm for vergasovaite and 0.18×0.10×0.14 mm for synthetic analog were chosen and more than a

This is the peer-reviewed, final accepted version for American Mineralogist, published by the Mineralogical Society of America.
The published version is subject to change. Cite as Authors (Year) Title. American Mineralogist, in press.
DOI: https://doi.org/10.2138/am-2022-8753. http://www.minsocam.org/

hemisphere of data was collected for each crystal with a frame width of 0.5° in ω, and 2 s spent counting for each frame. The data were integrated and corrected for absorption applying a multiscan type model using the Rigaku Oxford Diffraction programs CrysAlis Pro. For each crystal, a complete data set was collected in the 300–1150 K range using a hot air gas blower system. During the experiment, the crystal was fixed in a quartz capillary in an upright position using a quartz fiber. Initially, the temperature step was 25 K; for a more detailed study of the 300 – 800 K interval for a mineral, the step was decreased to 10 K. The atomic coordinates for synthetic cupromolybdite (treating one site as sulfur-occupied) published by Vilminot et al. (2009) were used as starting point, and the structure was successfully refined with the use of SHELX software package (Sheldrick 2015).

Both for the vergasovaite mineral sample and for the synthetic one, the experiments were repeated on other crystals to make sure that there were no possible artifacts when performing the X-ray study. The results below are represented for one sets of the experiments for each type of material, since they show good reproducibility.

Table 2. Crystallographic data for vergasovaite (***VM***) and its synthetic analog (***SA***) at 300 K.

	VM	***SA***
Space group	*Pnma*	*Pnma*
a(Å)	7.4304(3)	7.4295(3)
b(Å)	6.8154(2)	6.8293(3)
c(Å)	13.5310(6)	13.5087(5)
V(Å^3)	685.23(5)	685.41(5)
Θ max, °	3.35	3.34
	29.45	25.24
No. of measured	896	1256
and independent	782	1102
reflections		
R_{int}	0.048	0.039
R_{Σ}	0.039	0.039
wR_1	0.049	0.061
R_1	0.022	0.027
S	1.094	1.057

3. Results

3.1 Crystal structure

3.1.1 Vergasovaite mineral sample (VM)

In the studied sample of ***VM*** mineral, the *T*1 site has a mixed refined $Mo_{0.947(4)}S_{0.053(4)}$ occupancy, whereas *T*2 is fully occupied by sulfur. Vanadium content unambiguously determined by microprobe cannot be refined. Atomic coordinates and thermal displacement parameters for ***VM*** for each temperature are provided in the corresponding Crystallographic

Information Files (CIFs) (Supplement). At 300 K, ***VM*** is orthorhombic, *Pnma*, a = 7.4304(3), b = 6.8154(2), c = 13.5310(6) Å, V = 685.23(5) Å^3 (Table 2). According to the chemical analysis in Table 1, the occupancy of the $T1$ site is $Mo_{0.91}S_{0.08}V_{0.04}$.

The crystal structure is refined to the reasonable values in the temperature range of 300 – 975 K (R_1 = 2.5 – 5.5%, S ~ 1.00). At 1000 – 1050 K, only cell parameters could be calculated, while at 1075 K, the structure is well refined with both T sites completely occupied by Mo atoms only, i.e. as isostructural to that of cupromolybdite down to R_1 = 5.32% and S = 0.995. There are also significant changes in the data quality are observed with the rise of the temperature; below 975 K $R_{int} \leq 5\%$, while at 1000 K, R_{int} = 68.09%, at 1025 K - 16.97%, at 1050 K - 27.08%. At 1075 K, R_{int} value decreases to 9.56% and later again increases to 19.63% at 1100 K. It took 10 minutes for the thermal equilibration of the crystal at each point in the 500 – 1100 K range and 15 minutes at 300 – 500 K range.

In the crystal structures of vergasovaite and its synthetic analogue, oxocentered OCu_4 tetrahedra share vertices to form chains (Fig. 2 a,c), which in turn are interconnected into the 3D framework by the sulfate and molybdate anions (Berlepsch et al. 1999). The unit-cell contains three symmetrically independent copper sites (Fig. 2d), whereof two, Cu1 and Cu3, are coordinated in a strongly distorted octahedral motif while the third, Cu2, in square pyramidal (considering Cu-O distances below 3.5 Å). Cu1 and Cu3 sites form four long (2.054(4) – 2.376(3) Å) and two short (1.898(2) – 1.935(4) Å) bonds each, which is rather uncommon. A similar coordination was also observed for Cu^{2+} in the structures of $CuMoO_4$ (Soltys et al. 2018) and in Cu-doped $Zn_3O(MoO_4)_2$ (Sohnel et al. 1996). Cu [4+2] coordination is also observed in the structure of volborthite (Basso et al. 1988), wherein Cu1 atom forms four long equatorial bonds of 2.172(6) Å, and two short apical bonds of 1.938(6) Å. A significant amount of Zn determined by microprobe (Table 1) is substituting for Cu in vergasovaite. The exact amount of Zn in each of three Cu sites, in vergasovaite, cannot be refined, due to the very poor Cu/Zn scattering contrast by XRD.

3.1.2 Synthetic analog (SA)

In contrast to the mineral sample (***VM***), Mo and S are completely ordered with $T1$ site occupied by molybdenum and $T2$ site occupied exclusively by sulfur. Atomic coordinates and thermal displacement parameters for the ***SA*** for each temperature in the range 300-700 K are given in the Crystallographic Information Files (CIFs) (Supplement). At 300 K, ***SA*** is orthorhombic, space group *Pnma*, a = 7.4295(3), b = 6.8293(3), c = 13.5087(5) Å, V = 685.41(5) Å^3 (Table 2). In sharp contrast to the ***VM***, ***SA*** is stable only until 700 K above which it darkens and becomes amorphous. At all points, the structure could be refined down to acceptable values of R_1 = 2.7 – 5.7%, S ~ 1.00.

This is the peer-reviewed, final accepted version for American Mineralogist, published by the Mineralogical Society of America.
The published version is subject to change. Cite as Authors (Year) Title. American Mineralogist, in press.
DOI: https://doi.org/10.2138/am-2022-8753. http://www.minsocam.org/

3.2 High-temperature transformations

3.2.1 Transformation pathways

Vergasovaite mineral sample (VM)

Upon heating to 900 K, the initial green color of the crystal is retained, but at 925 K (Fig. 3) it turns reddish; the crystal shape is preserved. At 975 K (Fig. 3c), the crystal facets are clearly visible. At 1000 K, the crystal habit is retained but the facets look somewhat smeared (Fig. 3d); at 1025 K (Fig. 3e), a drop of melt is clearly visible. The composition of the melt drop corresponds approximately to dolerophanite $Cu_2O(SO_4)$ as determined by microprobe analysis. Brownish red color of the resulted crystal after transformation of ***VM*** coincides with the color of cupromolybdite (Zelenski et al. 2012).

Reconstruction of the reciprocal space of ***VM*** (Fig. 3 a,b) indicates only smooth changes in the crystal in the 300-950 K range. At 975 K, a sphere of additional reflections appears indicating the beginning of transformation; an abrupt change of cell metrics is also observed (Fig. 5a). No variation in occupancies of tetrahedral sites is observed below 950 K; the mean bond lengths are <d(Mo-O)> = 1.746 Å and <d(S-O)> = 1.460 Å at this temperature. At 975 K, both tetrahedral sites become occupied exclusively by molybdenum while sulfur is no longer present; the mean bond lengths are <d(*T*1-O)> = 1.748 Å and <d(*T*2-O)> = 1.735 Å.

At 975 K, the initial vergasovaite $Cu_3O(MoO_4)(SO_4)$ transforms into cupromolybdite $Cu_3O(MoO_4)_2$. The process is so fast that the crystal retains its initial shape and only the color change is observed by a naked eye. The changes invoked by "desulfurization" manifest themselves at essentially higher temperatures. At 975 K, the diffraction pattern contains some extra reflections besides those of cupromolybdite. Unfortunately, this pattern does not permit to determine the cell parameters of the "extra" phase. It is necessary to note that with the temperature rise the diffraction maxima do not vanish which indicates that the crystal is not completely destroyed. At 1075 K, the 'extra' maxima are almost extinct (Fig. 3f); at 1100 K, there are further changes which correlate with the reference data on thermal decomposition of $Cu_3Mo_2O_9$ at 1110 – 1130 K (Machej and Ziołkowski 1980; Nassau and Schiever 1969; Kohlmuller and Faurie 1967).

Synthetic analogue (SA)

Contrary to the mineral sample, the crystal of the synthetic compound does not undergo the transformation described above; it decomposes completely at as low temperature as 700 K with no indication to (re)crystallization at least below 1200 K. The occupancies of the tetrahedral position are not varied with temperature; there are also no visible changes in the reciprocal space. The orientation matrix remains constant until the melting point.

This is the peer-reviewed, final accepted version for American Mineralogist, published by the Mineralogical Society of America.
The published version is subject to change. Cite as Authors (Year) Title. American Mineralogist, in press.
DOI: https://doi.org/10.2138/am-2022-8753. http://www.minsocam.org/

Upon heating, the crystal of ***SA*** changes its color from olive green to black (Fig. 4). Already at 650 K, darkening of the crystal is clearly visible; at 675 K, traces of black sublimate appear in the inner walls of the quartz capillary which clearly indicates the start of decomposition. At 700 K, the capillary becomes dull, with a black spot at the place where the crystal used to be. At 300 K, the reciprocal space contains only regular maxima; at 650 K, their number decreases sharply while the order is yet retained. At 675 K, a spheroid of reflections is observed indicating decay of the crystal. At 700 K, just a handful of spots are observed which totally disappear over time.

3.2.2 Unit-cell parameters and thermal expansion

Vergasovaite mineral sample (VM)

As follows from Fig. 5a, there are abrupt changes in evolution of unit-cell parameters at 950-975 K, which corresponds to the transformation into cupromolybdite. At 950 K, the unit cell parameters are a = 7.5241(8), b = 6.8411(6), c = 13.7591(14) Å, V = 708.22(12) Å^3, while at 975 K a = 7.7513(7), b = 6.8987(6), c = 14.6894(15) Å, V = 785.50(13) Å^3.

To verify high-temperature transformation pathway of vergasovaite, three consecutive experiments were conducted with different steps all showing almost identical behaviour of the material. The red dots in Figure 6a indicate datasets used for the fits. The thermal dependence of a, c and V of ***VM*** below 950 K can be approximated by a linear fit, while that for b is better approximated by a two-degree polynomial fit (Fig. 5a). The approximation equations at 300-950 K are as follows:

$a(t)=7.391+1.39\times10^{-4}t$;

$b(t)=6.851-1.58\times10^{-4}t+1.506\times10^{-7}t^2$;

$c(t)=13.440+3.429\times10^{-4}t$;

$V(t) = 674.55 + 0.03446t$.

The thermal expansion (TE) of the mineral is strongly anisotropic (Fig. 2f). Between 300 and 950 K, the main values of the TE tensor are $\alpha_{11}\times10^{-6}$ = 18.48…18.71 K^{-1}, $\alpha_{22}\times10^{-6}$ = -10.0…18.7 K^{-1}, $\alpha_{33}\times10^{-6}$ = 24.91…25.32 K^{-1}. In fact, the thermal expansion is more or less uniform along a and c while along b, the structure expands continuously until 950 K. The most likely reason for this behavior is the rigidity of the OCu_4 tetrahedra forming the $[O_2Cu_6]^{8+}$ chains running along the b axis. In the ab and bc planes, thermal expansion is minimal at low temperatures along these chains and increases slightly at elevated temperatures. In the ac plane, thermal expansion is nearly constant until 950 K; so is the volume expansion coefficient ($\alpha_V\times10^{-6}$ = 34.1…62.1 K^{-1}).

Synthetic analogue (SA)

This is the peer-reviewed, final accepted version for American Mineralogist, published by the Mineralogical Society of America.
The published version is subject to change. Cite as Authors (Year) Title. American Mineralogist, in press.
DOI: https://doi.org/10.2138/am-2022-8753. http://www.minsocam.org/

The thermal dependences of unit cell parameters exhibit one inflection and one kink (Fig. 5b). These parameters increase in the 300 – 450 K range while decrease slightly between 450 and 550 K. The kink is observed between 550 and 575 K. We could not reveal a structural reason for this observed phenomenon. The approximation equations for 300-550 K (a_1, b_1, c_1, V_1) and 575-700 K (a_2, b_2, c_2, V_2) are as follows:

$a_1(t)=7.180+1.211\times10^{-3}t-1.325\times10^{-6}t^2$; (for 300-550 K)

$a_2(t)=9.116-5.173\times10^{-3}t+4.074\times10^{-6}t^2$; (for 575-700 K)

$b_1(t)=6.673+8.031\times10^{-4}t-1.02\times10^{-6}t^2$;

$b_2(t)=8.519-5.229\times10^{-3}t+4.016\times10^{-6}t^2$;

$c_1(t)=12.944+2.732\times10^{-3}t-2.923\times10^{-6}t^2$;

$c_2(t)=16.871-10.29\times10^{-2}t+8.171\times10^{-6}t^2$;

$V_1(t)=616.331+3.397\times10^{-2}t-3.837\times10^{-4}t^2$;

$V_2(t)=1180.43-1.522t+1.192\times10^{-3}t^2$.

3.2.3 Bond lengths

The effect of thermal motion on the bond-lengths values from single-crystal X-ray diffraction experiment is well-known (Downs 2000). Corrections for all bonds discussed below in ***VM*** and ***SA*** were calculated by using a formula for the rigid-body motion:

$$L^2 = l_0^2 + {}^3/_8\,\pi^2(\mathrm{B_{eq}}(A_2) - \mathrm{B_{eq}}(A_1)),$$

where L and l_0 are corrected and observed $A1$-$A2$ bond lengths, respectively; $B_{eq}(A1)$ and $B_{eq}(A2)$ are equivalent temperature factors of $A1$ (cation, i.e. Cu, S, Mo) and $A2$ (anion i.e. O) atoms, respectively.

The thermal dependences of the bond lengths in ***VM*** (Fig. 6) and ***SA*** (Fig. 7) are similar. Changes in the bond lengths in the oxocentered OCu_4 tetrahedra (Fig. 2d) with increasing temperature are comparable with the accuracy of determining the bond lengths. With increasing temperature 300 → 950 K, two O1-Cu1 bonds change from 1.8965(1) to 1.8900(1) Å, O1-Cu2 elongate from 1.9256(1) to 1.9438(1) Å, and O1-Cu3 changes from 1.9350(1) to 1.9435(1) Å in ***VM***. For example, dependences of the bond lengths *vs*. temperature for O1-Cu1 and O1-Cu3 bonds are shown in Figure 6 and 7.

A similar trend is observed for the molybdate and sulfate tetrahedra below 850 K (Fig. 6). The maximal elongation of the Mo-O and S-O bonds does not exceed 0.02 Å and 0.04 Å, respectively. At 850-950 K, these dependences significantly deviate from linearity, particularly for $T2$-O2 and $T1$-O6.

The changes of bond lengths in the cation centered $Cu2O_5$ and $Cu3O_6$ are relatively small (±0.06 Å) approaching 0.1 Å only for Cu3-O3 (difference in the bond length value at 950 and 300 K). Expansion of $Cu1O_6$ octahedron is more anisotropic. This polyhedron is formed by three pairs of bonds, Cu1-O1, Cu1-O4, and Cu1-O5 which change by -0.01, 0.14, and -0.11 Å, respectively. The most rigid Cu1-O1 bonds align parallel to the axes of $[Cu_3O]^{4+}$ chains while Cu1-O4 and Cu1-O5 are normal to them.

Comparison of the bond lengths in the structures of cupromolybdite, vergasovaite, and the product of its thermal transformation (Table 3) indicates that the differences for the $Cu1O_6$ and $Mo1O_4$ polyhedra do not exceed 0.07 Å. In $Cu2O_5$, a principal difference is observed only for Cu2-O3 (0.094 Å); the largest disagreement is observed for $Cu3O_6$ which exhibit two short and four long bonds. The short Cu3-O7 and Cu3-O3 bonds differ by 0.092 and 0.067 Å, respectively while four long bonds, when proceeding from vergasovaite to cupromolybdite, increase essentially: Cu3-O6, by 0.024 Å, Cu3-O2, by 0.049 Å, and Cu3-O4, by 0.047 Å.

Table 3. Bond-distance values in the structures of vergasovaite, the product of its chemical transformation (cupromolybdite), synthetic analog of vergasovaite, and cupromolybdite mineral.

	Vergasovaite 300 K (this study)	Vergasovaite synthetic analog 300 K (this study)	Vergasovaite synthetic analog 950 K***	Cupromolybdite after the transformation of vergasovaite at 975 K (this study)***	Cupromolybdite mineral (Zelenski et al., 2012)
Cu1-O1 ×2	1.8977(16)	1.9041(14)	1.8990(1)	1.8675(1)	1.8606(14)
Cu1-O4 ×2	2.094(3)	2.082(2)	2.2633(1)	2.2571(1)	2.186(3)
Cu1-O5 ×2	2.376(3)	2.386(2)	2.2574(1)	2.2676(1)	2.257(3)
Cu2-O1	1.929(4)	1.928(3)	1.9300(1)	1.9467(1)	1.930(3)
Cu2-O2	1.935(4)	1.936(3)	1.9685(1)	1.9412(1)	1.884(4)
Cu2-O5 ×2	1.957(3)	1.955(2)	2.0266(1)	2.0701(1)	1.992(2)
Cu2-O3	2.526(4)	2.540(3)	2.4880(1)	2.2543(1)	2.160(4)
Cu3-O7	1.896(4)	1.900(3)	1. 9602(1)	2.0451(1)	1.953(4)
Cu3-O1	1.935(4)	1.926(3)	1.9459(1)	1.9991(1)	1.950(3)
Cu3-O6	2.054(4)	2.050(3)	2.1143(1)	2.3600(1)	2.336(4)
Cu3-O3	2.162(4)	2.154(4)	2.2935(1)	2.6257(1)	2.559(5)
Cu3-O4 ×2	2.264(3)	2.275(2)	2.2846(1)	2.0639(1)	2.016(3)
*T*1*-O6	1.718(4)	1.722(3)	1.7410(1)	1.7428(1)	1.709(4)

This is the peer-reviewed, final accepted version for American Mineralogist, published by the Mineralogical Society of America.
The published version is subject to change. Cite as Authors (Year) Title. American Mineralogist, in press.
DOI: https://doi.org/10.2138/am-2022-8753. http://www.minsocam.org/

*T*1*-O7	1.745(4)	1.743(4)	1.7562(1)	1.7818(1)	1.759(4)
*T*1*-O5 ×2	1.775(3)	1.782(2)	1.8015(1)	1.7964(1)	1.787(2)
*T*2**-O2	1.471(5)	1.467(4)	1.5054(1)	1.8105(1)	1.734(4)
*T*2**-O3	1.477(4)	1.472(4)	1.5193(1)	1.7716(1)	1.713(4)
*T*2**-O4 ×2	1.484(3)	1.486(2)	1.5040(1)	1.7709(1)	1.767(3)

*T1 = Mo^{6+} (predominantly) in vergasovaite and cupromolybdite; **T2 = S^{6+} in vergasovaite, whereas T2 = Mo^{6+} in cupromolybdite; *** bond-distance values obtained after the correction using a formula for the rigid-body motion.

Concluding remarks

Vergasovaite is stable until 950 K. Between 950 and 975 K, the unit-cell parameters change abruptly as vergasovaite transforms into cupromolybdite with expulsion of sulfur but without destruction of the crystal shape. The structural changes upon heating are very similar for the natural vergasovaite and its synthetic analog, yet their decomposition points change drastically. Most probable explanation is the stabilization of the mineral structure by the admixtures of Zn and V at the Cu and Mo sites, respectively. It is worth noting that the compound $Cu_3O(MoO_4)_2$ is commonly formed as a product of high-temperature decomposition of some other copper molybdates, e.g lindgrenite, $Cu_3(MoO_4)_2(OH)_2$, and szenicsite, $Cu_3(MoO_4)(OH)_4$ (Ismagilova et al. 2019). For the thermal decomposition of vergasovaite, one can suggest the following schematic reaction: $2Cu_3O(MoO_4)(SO_4) = Cu_3O(MoO_4)_2 + \{CuSO_4 + Cu_2OSO_4\}$, the species in braces forming the melt, as in the studied case. Additional sealed-tube experiments also suggest relative volatility of $Cu_2O(SO_4)$, most likely due to chemical transport: upon heating the mixtures of anhydrous $CuSO_4$ and pre-synthesized Cu_2OSO_4 and $Cu_3Mo_2O_9$ in the 770 – 1150 K temperature range, red-brown single crystals of Cu_2OSO_4 are first to form; they are also observed on the tube walls above the main charge which suggests vapor growth mechanism to be at least partly operative. The role of trace admixtures like Zn and V in preservation of the initial crystal is yet to be understood, but most likely important as demonstrated by simple melting of the zinc- and vanadium-free crystal of the synthetic analog. The current study shows that it is impossible to predict the properties obtained on minerals for synthetic compounds and *vice versa*. At the same time, zinc and/or vanadium doping of synthetic analogues of vergasovaite can have a decisive effect on the manifestation of nontrivial properties in the studied series of compounds.

Upon heating the mineral and its synthetic analog demonstrate significantly different behavior. The largest increase is observed for the ***c*** parameter (by 0.13 and 0.17 Å, respectively)

This is the peer-reviewed, final accepted version for American Mineralogist, published by the Mineralogical Society of America.
The published version is subject to change. Cite as Authors (Year) Title. American Mineralogist, in press.
DOI: https://doi.org/10.2138/am-2022-8753. http://www.minsocam.org/

in both materials. In the structure for the mineral (Table. 4), the *a* and *b* increase by a similar value (0.1 and 0.09 Å), while virtually no change in *b* is observed (0.002 Å) for the synthetic $Cu_3O(SO_4)(MoO_4)$. Upon further heating of the transformation product, the cupromolybdite structure is stabilized, which is reflected at 1075 K by increasing quality of the diffraction pattern; the compound starts melting at 1100 K.

Table 4. Unit-cell parameters at ambient and at temperatures of decomposition for the vergasovaite and its synthetic analog.

	Vergasovaite		Increment	Synthetic analogue		Increment
	300K	950K		300K	700K	
a (Å)	7.421(2)	7.5241(8)	0.1031	7.4295(3)	7.4944(4)	0.0649
b (Å)	6.754(3)	6.8411(6)	0.0871	6.8293(3)	6.8277(3)	-0.0016
c (Å)	13.624(5)	13.7591(14)	0.1351	13.5087(5)	13.6776(6)	0.1689
V (Å^3)	682.85(3)	708.22(12)	25.37	685.41(5)	699.88(6)	14.47

In the structure of vergasovaite, the sulfate and molybdate tetrahedra, as well as the OCu_4 species, are strong and rigid constituents, which remain almost unchanged during heating (Fig. 6, 7). The same is also observed for the $Cu2O_5$ square pyramids. The peculiarities of the thermal expansion of vergasovaite can be explained by the anisotropy of bond length evolution in the $Cu1O_6$ and $Cu3O_6$ octahedra and flexibility of the Mo(*T*1)-O-Cu and S(*T*2)-O-Cu bond angles (Fig. 8). Copper polyhedra with higher coordination numbers are easier to transform upon temperature increase. The weakest expansion is observed along the $[O_2Cu_6]^{8+}$ chains.

By now, the fumaroles of Tolbachik are known to produce three minerals with the overall $A_3O(SO_4)(TO_4)$ formula (*A* = Cu, Zn; *T* = S, Mo): glikinite, $Zn_3O(SO_4)_2$ (Nazarchuk et al., 2020), vergasovaite, $Cu_3O(SO_4)(MoO_4)$, and cupromolybdite, $Cu_3O(MoO_4)_2$. By now, synthetic analogs have been produced for all three (Bald and Grühn, 1981; Vilminot et al., 2009; this work). The formation temperatures reported, 1140 K (Kihlborg et al., 1971) to 875 K (Steiner et al, 1996, 1997; Bald et al., 1981), are very close to those observed in the GTFE fumaroles. The crystal structures of these three minerals and their synthetic analogs are based on the $[A_3O]^{2+}$ (*A* = Cu, Zn) chains which are also present in the structure of kamchatkite $KCu_3O(SO_4)_2Cl$ (Siidra et al., 2017). Considering the structural similarities of glikinite, vergasovaite and cupromolybdite and similarity of their formation conditions, one is tempted to assume the existence of a $Cu_3O(SO_4)_2$ mineral. Yet, no such compound has been reported; our attempts to prepare it have also been unsuccessful. However, it can probably be stabilized by doping. The structure of hermannjahnite, $CuZn(SO_4)_2$ (space group $P2_1/n$) (Siidra et al. 2016), indicates that exchange between copper and zinc sites may change the overall symmetry of the structure.

Implications

Synthetic $Cu_3O(MoO_4)_2$ and $CuMoO_4$ are employed as heterogeneous oxidation catalysts (Toniolo et al. 2008; Wang et al. 1998, 2002; Drummer et al. 2022). The latter compound has been suggested as a constituent of sensors (Li et al. 2019). It also exhibits magnetic ordering (Matsumoto el al. 2012; Kuroe et al. 2014). Partial replacement of MoO_4^{2-} by smaller SO_4^{2-} results in shortening of $Cu^{2+}\cdots Cu^{2+}$ contacts which is expected to enhance the magnetic exchange between these ions; hence, magnetic properties of synthetic vergasovaite are expected to be quite interesting. The topotactic transformation observed for vergasovaite in this work may bring new ideas and become an exciting playground for the preparation of self-regenerating compounds with such magnetic ions as Cu^{2+}. Flexible and diverse coordination of divalent copper cations is a contributing factor for such transformations. The copper-oxymolybdate framework is flexible enough to allow topotactic transitions to occur.

Whereas single-crystal-to-single-crystal transformations are studied in detail to date, well documented topotactic transitions in pure inorganic compounds with crystal shape preserving are as yet very rare. Observation of processes as reported above suggests more complex mechanisms and cascade of phenomena which allow preservation of the crystal. The transformation of vergasovaite into cupromolybdite with crystal shape preservation proceeds with a loss of volume and should lead to the formation of "spongy"-type structures described by Glikin (2009). The formation of the latter may occur only in the systems containing isomorphic components. Physically, the replacement of a protocrystal (usually, with a liquid phase presence) is accompanied by the inheritance of its structural fragments, which determine the preservation of the initial shape of crystals. This nonequilibrium process is associated with abrupt changes in the system. Probably, the first drops of the melt inside the natural vergasovaite crystals were the catalysts of the replacement process, which took place simultaneously with the "desulfurization".

The transformation of vergasovaite into cupromolybdite demonstrates the complexity of the processes in the fumaroles of the scoria cones of the Tolbachik volcano with an exceptionally rich mineral diversity. The temperature regime in active fumaroles is not constant and changes by hundreds of degrees Celsius depending on volcanic activity, which in turn causes the transformation of minerals and the emergence of new ones. Understanding the various processes and knowledge of the nature of the alteration products of divalent copper minerals are of interest for mineralogy, geochemistry and environmental science.

Acknowledgements

We are grateful to three anonymous reviewers for many valuable comments that significantly improved the initial version of the manuscript. Technical support by the SPbSU Resource Centers is gratefully acknowledged.

444

445 **References**

446 Badrtdinov, D.I., Kuznetsova, E.S., Verchenko, V.Yu., Berdonosov, P.S., Dolgikh, V.A.,
447 Mazurenko, V.V., and Tsirlin, A.A. (2018) Magnetism of coupled spin tetrahedra in
448 ilinskite-type $KCu_5O_2(SeO_3)_2Cl_3$. Scientific Reports, 8, 2379.

449 Bald, L., and Grühn, R. (1981) Die kristallstruktur von einem sulfat-reichen oxidsulfat des zinks.
450 Naturwissenschaften, 68, 39–39.

451 Balić-Žunić, T., Birkedal, R., Katerinopoulou, A., Comodi, P. (2016) Dehydration of blödite,
452 $Na_2Mg(SO_4)_2(H_2O)_4$, and leonite, $K_2Mg(SO_4)_2(H_2O)_4$. European Journal of Mineralogy,
453 28, 33-42.

454 Ballirano, P. (2015) Thermal behaviour of alum-(K) $KAl(SO_4)_2 \cdot 12H_2O$ from in situ laboratory
455 high-temperature powder X-ray diffractiondata: thermal expansion and modelling of the
456 sulfate orientational disorder. Mineralogical Magazine, 79, 157-170.

457 Basso, R., Palenzona, A., and Zefiro, L. (1988) Crystal structure refinement of volborthite from
458 Scrava mine (Eastern Liguria, Italy). Neues Jahrbuch für Mineralogie, Monatshefte,
459 1988, 385–394.

460 Berlepsch, P., Armbruster, T., Brugger, J., Bykova, E.Y., and Kartashov, P.M. (1999) The
461 crystal structure of vergasovaite $Cu_3O[(Mo,S)O_4SO_4]$, and its relation to synthetic
462 $Cu_3O[MoO_4]_2$. European Journal of Mineralogy, 11, 101–110.

463 Botana, A.S., Zheng, H., Lapidus, S.H., Mitchell, J.F., and Norman, M.R. (2018) A copper oxide
464 kagome antiferromagnet. Physical Review B: Condensed Matter, 98, 054421.

465 Bykova, E.Y., Berlepsch, P., Kartashov, P.M., Brugger, J., Armbruster, T., and Criddle, A.J.
466 (1998) Vergasovaite $Cu_3O[(Mo,S)O_4][SO_4]$, a new copper-oxy-molybdate-sulfate from
467 Kamchatka. Schweizerische Mineralogische und Petrographische Mitteilungen, 78, 479–
468 488.

469 Dent-Glasser, L.S., Glasser, F.P., and Taylor, H.F. W. (1962) Topotactic reactions in inorganic
470 oxycompounds. Quarterly Reviews Chemical Society, 16, 343–360.

471 Downs, R.T. (2000) Analysis of harmonic displacement factors. In: High-temperature and high
472 pressure crystal chemistry (Eds. R. M. Hazen, R. T. Downs). Reviews in Mineralogy and
473 Geochemistry, 41, 61–87.

474 Drummer, N.F., Sodiq-Ajala, Z., Morgan, D.J., and Davies, T.E. (2022) Investigating the
475 preparation of $Cu_3Mo_2O_9$ as a photocatalyst. Catalysis Communications, 163, 106414.

476 Fei H, Pham C.H., and Oliver S.R.J. (2012) Anion Exchange of the Cationic Layered Material
477 $[Pb_2F_2]^{2+}$. Journal of the American Chemical Society 134, 10729–10732.

Fujihala, M., Koorikawa, H., Mitsuda, S., Morita, K., Tohyama, T., Tomiyasu, K., Koda, A., Okabe, H., Itoh, S., Yokoo, T., Ibuka, S., Tadokoro, M., Itoh, M., Sagayama, H., Kumai, R., and Murakami, Y. (2017) Possible tomonaga-luttinger spin liquid state in the spin-1/2 inequilateral diamond-chain compound $K_3Cu_3AlO_2(SO_4)_4$. Scientific Reports, 7, 16785.

Glikin, A.E. (2009) Polymineral-Metasomatic Crystallogenesis. Springer Sciences (312 pp.).

Hara, S., and Sato, H. (2013) Structure and magnetism of novel copper molybdenum oxides η-$CuMoO_4$ and β-$Cu_3Mo_2O_9$. Journal of the Physical Society of Japan, 82, 054802.

Iordanidis, L., and Kanatzidis, M.G. (2000) Redox-induced "zipper" action in $Rb_2Bi_4Se_7$ and $Cs_2Bi_4Se_7$: Coupling of slabs to a three-dimensional framework through single-crystal to single-crystal conversion. Angewandte Chemie International Edition, 39, 1927–1930.

Ismagilova, R.M., Zhitova, E.S., Zolotarev, A.A., and Krivovichev, S.V. (2019) Jahn-Teller distortion and thermal expansion anisotropy: temperature-dependent behavior of lindgrenite, $Cu_3(MoO_4)_2(OH)_2$, szenicsite, $Cu_3(MoO_4)(OH)_4$, and cupromolybdite, $Cu_3O(MoO_4)_2$. Physics and Chemistry of Minerals, 46, 437–447

Kahlenberg, V., Braun, D.E., and Orlova, M. (2015) Investigations on alunogen under Mars-relevant temperature conditions: an example for a single-crystal-to-single-crystal phase transition. American Mineralogist, 100, 2548–2558.

Kihlborg, L., Norrestam, R., and Olivecrona, B. (1971) The crystal structure of $Cu_3Mo_2O_9$. Acta Crystallographica, B27, 2066–2070.

Kuroe, H., Aoki, K., Kino, R., Sato, T., Kuhawara, H., Sekine, T., Kihara, T., Akaki, M, Kohama, Y., Tokunaga, M., Matsuo, A., Kindo, K., Hase, M., Takehana, K., Kitazawa, H., Oka, K., Ito, T., and Eisaki, H. (2014) Magnetic and dielectric properties in multiferroic $Cu_3Mo_2O_9$ under high magnetic fields. JPS Conference Proceedings, 3, 014036

Li, J., Chen, X., Chen, S., Li, H., and Deng, H. (2019) A visible light induced ultrasensitive photoelectrochemical sensor based on $Cu_3Mo_2O_9/BaTiO_3$ p–n heterojunction for detecting oxytetracycline. Journal of Electroanalytical Chemistry, 842, 161–167.

Machej, T., and Ziołkowski, J. (1980) Subsolidus phase diagram of Cu_2O – CuO – MoO_3 system. Journal of Solid State Chemistry, 31, 135–143.

Matsumoto, M., Kuroe, H., Sekine, T., and Hase, M. (2012) Magnetic excitation and electric polarization in strongly coupled spin monomer and dimer system $Cu_3Mo_2O_9$. Journal of the Physical Society of Japan, 81, 024711.

Mentré, O., Blazquez-Alcover, I., Garcia-Martin, S., Duttine, M., Wattiaux, A., Simon, P., Huve, M., and Daviero-Minaud, S. (2018) Mixed-valence iron dumortierite $Fe_{13.5}^{2.22+}(As^{5+}O_4^{-}{}_x)_8(OH)_6$ and its intricate topotactic exsolution at mild temperatures. Inorganic Chemistry, 57, 15093–15104.

513 Mer, A., Obbade, S., Devaux, P., and Abraham, F. (2019) Structural evolution in the rare-earth
514 uranyl vanadates $Ln_2[(UO_2)_2V_2O_8]_3 \cdot nH_2O$, singularity of the lanthanum compound, and
515 single- crystal to single-crystal partial dehydration. Crystal Growth and Design, 19,
516 3305– 33145.
517 Müller, P., Wisser, F.M., Bon, V., Grünker, R., Senkovska, I., and Kaskel, S. (2015) Post-
518 synthetic paddle-wheel crosslinking and functionalization of 1,3-
519 phenylenebis(azanetriyl)tetrabenzoate based MOFs. Chemistry of Materials, 27, 2460–
520 2467.
521 Nassau, K., Shiever, J.W. (1969) Cupric oxide-molybdenum oxide phase diagram in air and in
522 oxygen. Journal of the American Ceramic Society, 52, 36-40.
523 Nazarchuk, E.V., Siidra, O.I., Nekrasova, D.O., Shilovskikh, V.V., Borisov, A.S., and
524 Avdontseva, E.Yu. (2020) Glikinite, $Zn_3O(SO_4)_2$, a new anhydrous zinc oxysulfate
525 mineral structurally based on OZn_4 tetrahedra. Mineralogical Magazine, 84, 563–567.
526 Neagu, D., Tsekouras, G., Miller, D.N., M´enard, H., and Irvine, J.T.S. (2013) In situ growth of
527 nanoparticles through control of non-stoichiometry. Nature Chemistry, 5, 916–923
528 Nekrasova, D.O., Tsirlin, A., Colmont, M., Siidra, O.I., Arevalo-Lopez, A., and Mentré, O.
529 (2021) From (s = 1) spin-hexamer to spin-tetradecamer by CuO interstitials in
530 $A_2Cu_3O(CuO)_x(SO_4)_3$, A = alkali. Inorganic Chemistry, 60, 18185–18191.
531 Nicol, A.W. (1963) Topotactic transformation of muscovite under mild hydrothermal conditions.
532 Clays and Clay Minerals, 12, 11–19.
533 Pekov, I.V., Agakhanov, A.A., Zubkova, N.V., Koshlyakova, N.N., Shchipalkina, N.V.,
534 Sandalov, F.D., Yapaskurt, V.O., Turchkova, A.G., and Sidorov, E.G. (2020) Oxidizing-type
535 fumaroles of the Tolbachik Volcano, a mineralogical and geochemical unique.
536 Russian Geology and Geophysics, 61, 675–688.
537 Pekov, I.V., Britvin, S.N., Yapaskurt, V.O., Krivovichev, S.V., Vigasina, M.F., and Sidorov,
538 E.G. (2021) Vasilseverginite, $Cu_9O_4(AsO_4)_2(SO_4)_2$, a new fumarolic mineral with a hybrid
539 structure containing novel anion-centered tetrahedral structural units. American
540 Mineralogist, 106, 633–640.
541 Peryshkov D.V., Popov A.A., and Strauss, S.H. (2010) Direct perfluorination of $K_2B_{12}H_{12}$ in
542 acetonitrile occurs at the gas bubble–solution interface and is inhibited by HF.
543 Experimental and DFT study of inhibition by protic acids and soft, polarizable anions.
544 Journal of the American Chemical Society, 132, 13902–13913.
545 Sahoo, S.C., Kundu, T., and Banerjee, R. (2011) Helical water chain mediated proton
546 conductivity in homochiral metal-organic frameworks with unprecedented zeolitic unh-
547 topology. Journal of the American Chemical Society, 133, 17950–17958.

548 Sheldrick, G.M. (2015) New features added to the refinement program SHELXL since 2008 are
549 described and explained. Acta Crystallographica Section C: Crystal Structure
550 Communications, 71, 3–8.
551 Siidra, O.I., Nazarchuk, E.V., Zaitsev, A.N., Lukina, E.A., Avdontseva, E.Y., Vergasova, L.P.,
552 Vlasenko, N.S., Filatov, S.K., Turner, R., and Karpov, G.A. (2017) Copper oxosulphates
553 from fumaroles of Tolbachik Vulcano: puninite, $Na_2Cu_3O(SO_4)_3$ a new mineral species
554 and structure refinements of kamchatkite and alumoklyuchevskite. European Journal of
555 Mineralogy, 29, 499–510.
556 Siidra, O.I., Nazarchuk, E.V., Agakhanov, A.A., and Polekhovsky, Y.S. (2019) Aleutite
557 $[Cu_5O_2](AsO_4)(VO_4)\cdot(Cu_{0.5}\square_{0.5})Cl$, a new complex salt-inclusion mineral with Cu^{2+}
558 substructure derived from Kagome-net. Mineralogical Magazine, 83, 847–853.
559 Siidra O.I., Vladimirova V.A., Tsirlin A.A., Chukanov N.V., and Ugolkov V.L. (2020)
560 $Cu_9O_2(VO_4)_4Cl_2$, the first copper oxychloride vanadate: mineralogically inspired
561 synthesis and magnetic behavior. Inorganic Chemistry, 59, 2136–2143.
562 Söhnel, T., Reichelt, W., Oppermann, H., Mattausch, H., and Simon, A. (1996) On the system
563 Zn/Mo/O. I. Phases and properties of ternary zinc molybdates; crystal structure of
564 $Zn_3Mo_2O_9$. Zeitschrift für Anorganische und Allgemeine Chemie, 622, 1274-1280.
565 Soltys, E.V., Urazov, Kh.Kh., Kharlamova, T.S., and Vodyankina, O.V. (2018) Redox and
566 catalytic properties of copper molybdates with various composition. Kinetika i Kataliz,
567 59, 79-91.
568 Steiner, U., Reichelt, W., and Oppermann, H. Z. (1996) Koexistenzbeziehungen, darstellung und
569 eigenschaften ternärer phasen im system Cu/Mo/O. Zeitschrift für Anorganische und
570 Allgemeine Chemie, 622, 1428-1434.
571 Steiner, U., and Reichelt, W. (1997) A reinvestigation of $Cu_3Mo_2O_9$, a compound containing
572 copper(II) in compressed octahedral coordination. Acta Crystallographica, C53, 1371-
573 1373
574 Thomas, I.D., Herzog, A., and Mclacnlan, D.Jr. (1956) The crystallography of two
575 compounds containing the oxides of copper and molybdenum. Acta Crystallographica
576 Section C: Crystal Structure Communications, 9, 316-317.
577 Toniolo, F.S., Barbosa-Coutinho, E., Schwaab, M., Leocadio, I.C., Aderne, R.S., Schmal, M.,
578 and Pinto, J.C. (2008) Kinetics of the catalytic combustion of diesel soot with MoO_3/Al_2O_3
579 catalyst from thermogravimetric analyses. Applied Catalysis A: General, 342, 87-92.
580 Vergasova, L.P., and Filatov, S.K. (1993) Volcanic exhalative minerals, a specific genetic group
581 (from data on the 1975-1976 Tolbachik eruption). Zapiski VMO, 4, 68-76

582 Vergasova, L.P., and Filatov, S.K. (2016) A study of volcanogenic exhalation mineralization.
583 Journal of Volcanology and Seismology, 10, 71-85.
584 Vilminot, S., André, G., and Kurmoo, M. (2009) Magnetic properties and magnetic structure of
585 $Cu^{II}_3Mo^{VI}_2O_9$. Inorganic Chemistry, 48, 2687-2692
586 Wang, X., Zhang, H., Sinkler, W., Poeppelmeier, K.R., and Marks, L.D. (1998) Reduction of
587 magnesium orthovanadate $Mg_3(VO_4)_2$. Journal of Alloys and Compounds, 270, 88-94.
588 Wang, C.H., Lee, C.N., and Weng, H.S. (1998) Effect of acid treatment on the performance of
589 the $CuO\text{-}MoO_3/Al_2O_3$ catalyst for the destructive oxidation of $(CH_3)_2S_2$. Industrial &
590 Engineering Chemistry Research, 37, 1774-1780.
591 Wang, C.H., Lin, S.S., Liou, S.B., and Weng, H.S. (2002) The promoter effect and a rate
592 expression of the catalytic incineration of $(CH_3)_2S_2$ over an improved $CuO\text{-}MoO_3/\gamma\text{-}$
593 Al_2O_3 catalyst. Chemosphere, 49, 389-394.
594 Zelenski, M.E., Zubkova, N.V., Pekov, I.V., Polekhovsky, Y.S., and Pushcharovsky, D.Yu.
595 (2012) Cupromolybdite, $Cu_3O(MoO_4)_2$, a new fumarolic mineral from the Tolbachik volcano,
596 Kamchatka Peninsula, Russia. European Journal of Mineralogy, 24, 749-75
597
598
599 **Figure captions**
600
601 **Figure 1.** Olive-green crystals of vergasovaite in association with langbeinite (white) and
602 euchlorine (light-green) (a) and crystals of synthetic vergasovaite obtained in an open silica tube
603 (b).
604
605
606 **Figure 2**. General projection of the crystal structure of vergasovaite (a-c) (OCu_4 tetrahedra =
607 orange, S = yellow balls, Mo = green balls, Cu = blue balls, O = red balls). The coordination of
608 the cations and the "additional" oxygen anion at 300 K (d). The shifts of atoms in vergasovaite
609 (***VM***) upon heating (e). Projections of thermal expansion tensors for vergasovaite (***VM***) (f).
610 Negative thermal expansion is highlighted in red.
611
612 **Figure 3.** Evolution of the vergasovaite (***VM***) crystal color and reciprocal space upon continuous
613 heating in the temperature range from 300 to 1075 K. The crystal and sulfate melt drop are
614 encircled with the white dashed line for clarity. The data were acquired on a Rigaku XtaLAB
615 Synergy-S diffractometer.

616
617
618 **Figure 4.** Evolution of the synthetic analogue of vergasovaite (***SA***) crystal color and reciprocal
619 space upon continuous heating in the temperature range from 300 to 700 K. The crystal and
620 black melt are encircled with the dashed line for clarity. The data were acquired on a Rigaku
621 XtaLAB Synergy-S diffractometer.
622
623
624 **Figure 5**. Thermal dependence of unit-cell parameters for vergasovaite. Results of three
625 consecutive experiments vergasovaite (***VM***) are shown in different colors (blue, orange and red)
626 (a). Thermal dependence of unit-cell parameters for the synthetic analog of vergasovaite. Results
627 of two consecutive experiments for synthetic analog (***SA***) are shown in different colors (blue and
628 red) (b). Note, the error bars are smaller than the markers size.
629
630 **Figure 6.** Selected bond lengths *vs*. temperature in the structure of vergasovaite ***VM***. Note, the
631 error bars are smaller than the markers size.
632
633
634 **Figure 7.** Selected bond lengths *vs*. temperature in the structure of the synthetic analogue of
635 vergasovaite (***SA***). Note, the error bars are smaller than the markers size.
636
637
638 **Figure 8.** Evolution of the *T*1-O-Cu and *T*2-O-Cu bond angles upon continuous heating in the
639 structures of vergasovaite ***VM*** (blue) and the synthetic analogue (***SA***). The angle value changes
640 are labeled. Note, the error bars are smaller than the markers size.
641
642
643
644
645
646
647
648

This is the peer-reviewed, final accepted version for American Mineralogist, published by the Mineralogical Society of America.
The published version is subject to change. Cite as Authors (Year) Title. American Mineralogist, in press.
DOI: https://doi.org/10.2138/am-2022-8753. http://www.minsocam.org/

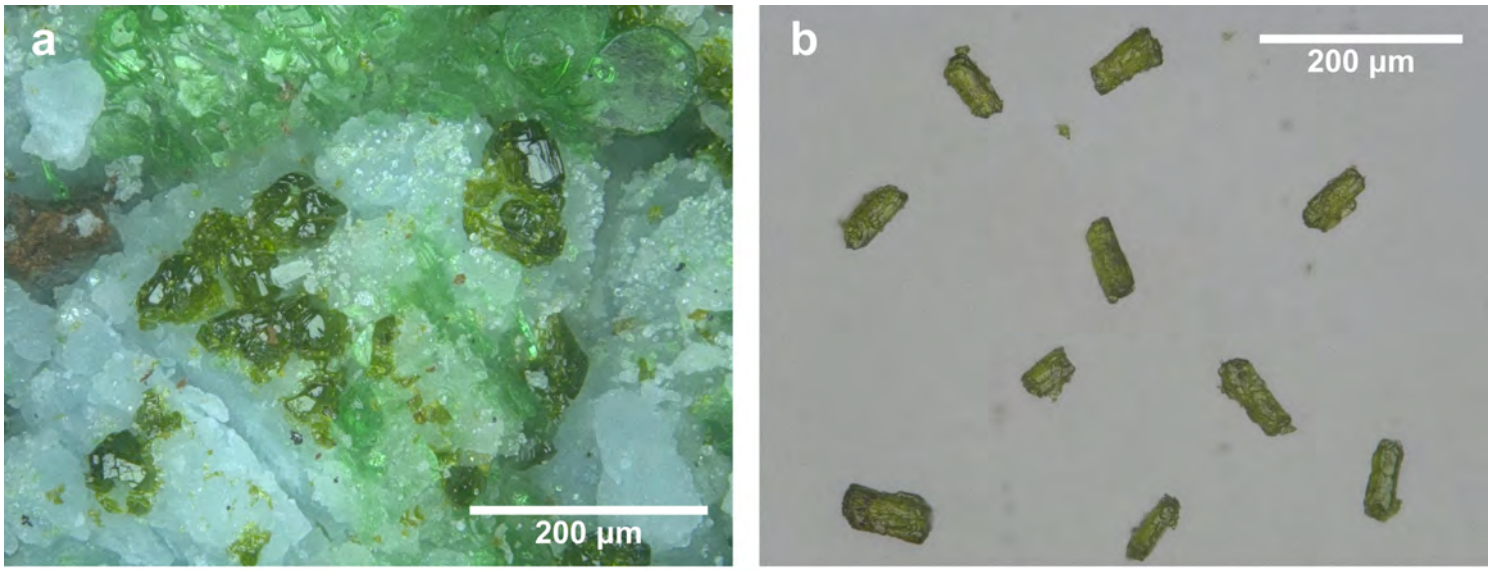

Figure 1

This is the peer-reviewed, final accepted version for American Mineralogist, published by the Mineralogical Society of America.
The published version is subject to change. Cite as Authors (Year) Title. American Mineralogist, in press.
DOI: https://doi.org/10.2138/am-2022-8753. http://www.minsocam.org/

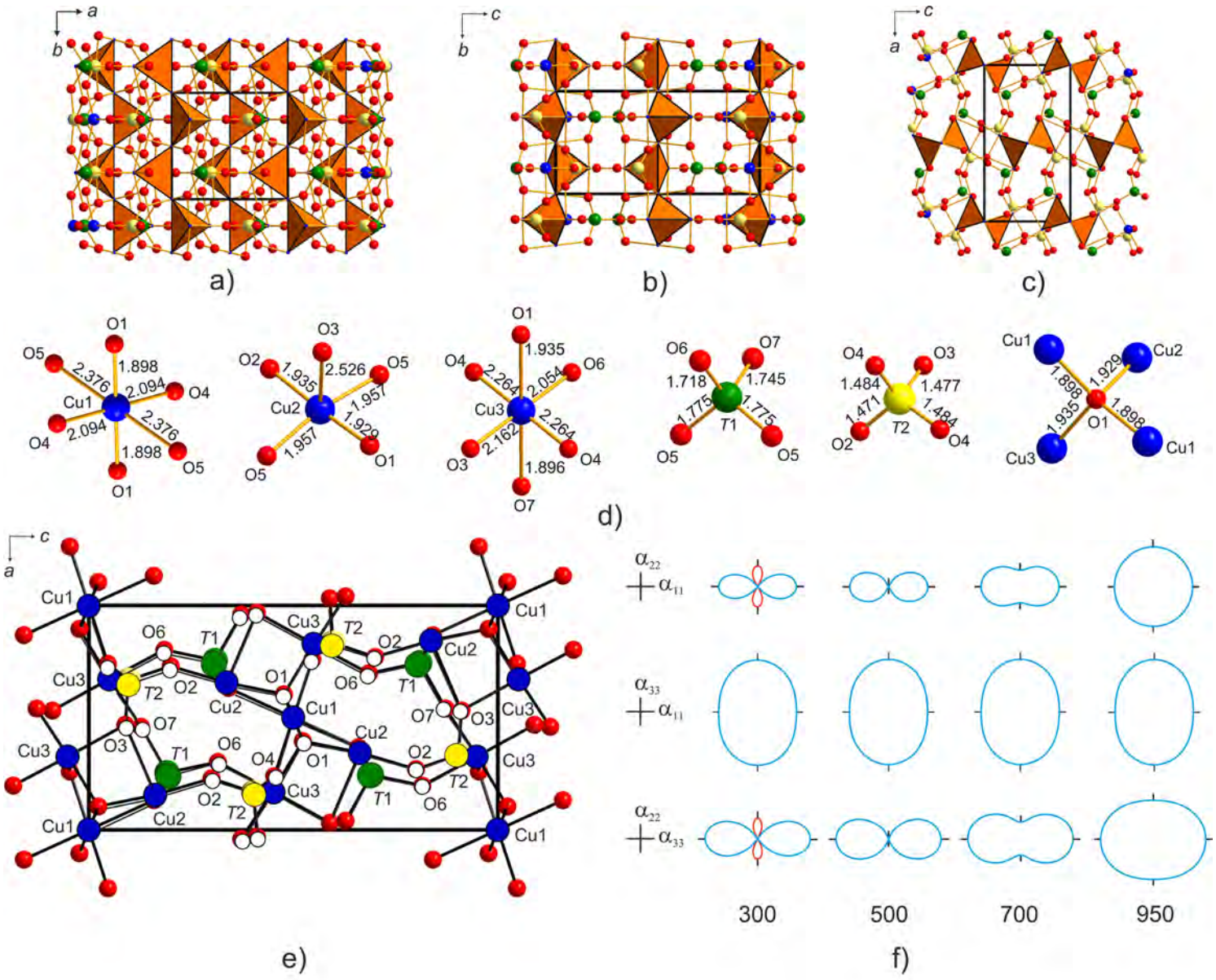

Figure 2

This is the peer-reviewed, final accepted version for American Mineralogist, published by the Mineralogical Society of America.
The published version is subject to change. Cite as Authors (Year) Title. American Mineralogist, in press.
DOI: https://doi.org/10.2138/am-2022-8753. http://www.minsocam.org/

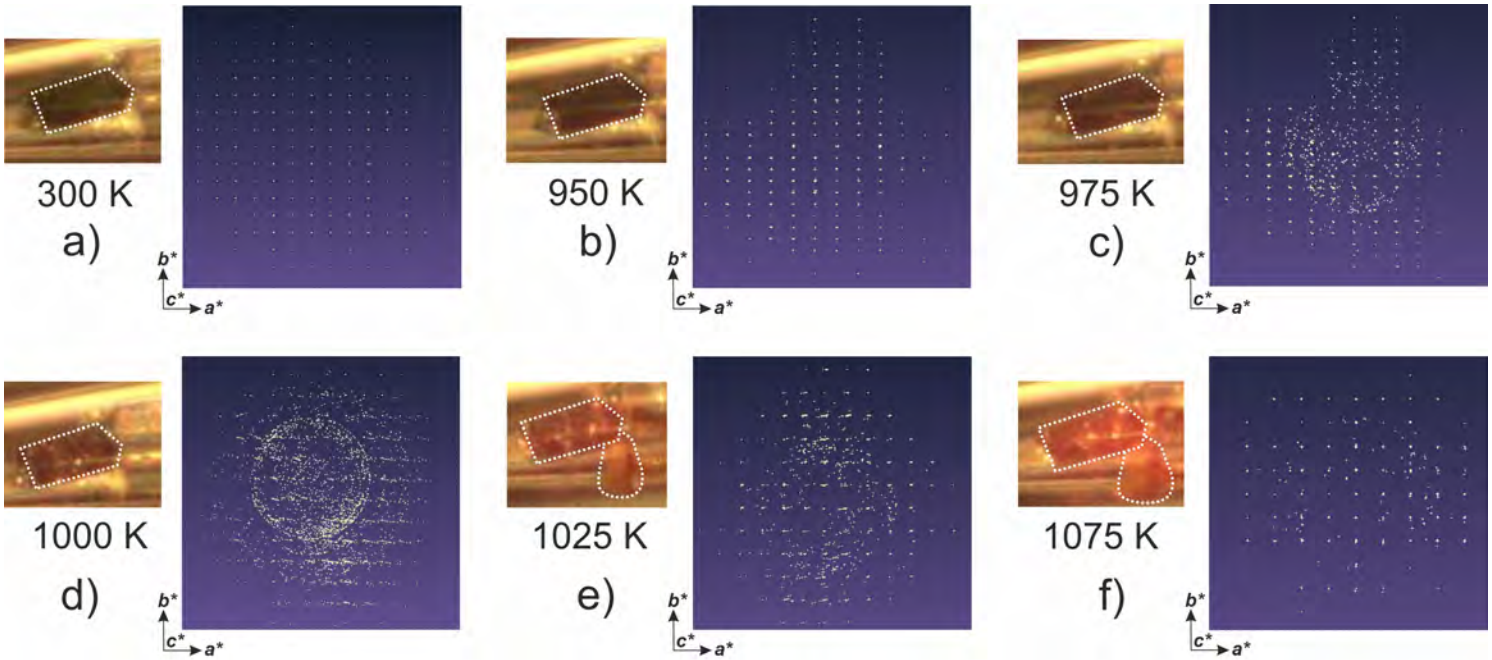

Figure 3

This is the peer-reviewed, final accepted version for American Mineralogist, published by the Mineralogical Society of America.
The published version is subject to change. Cite as Authors (Year) Title. American Mineralogist, in press.
DOI: https://doi.org/10.2138/am-2022-8753. http://www.minsocam.org/

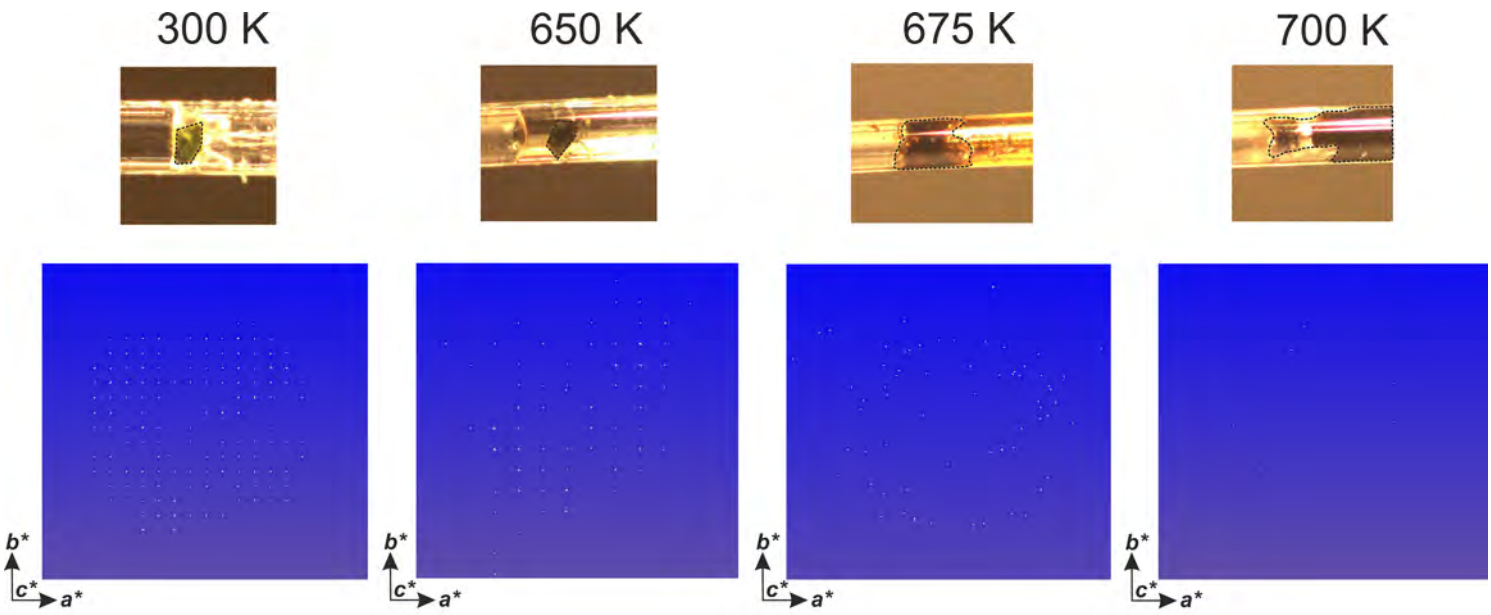

Figure 4

This is the peer-reviewed, final accepted version for American Mineralogist, published by the Mineralogical Society of America.
The published version is subject to change. Cite as Authors (Year) Title. American Mineralogist, in press.
DOI: https://doi.org/10.2138/am-2022-8753. http://www.minsocam.org/

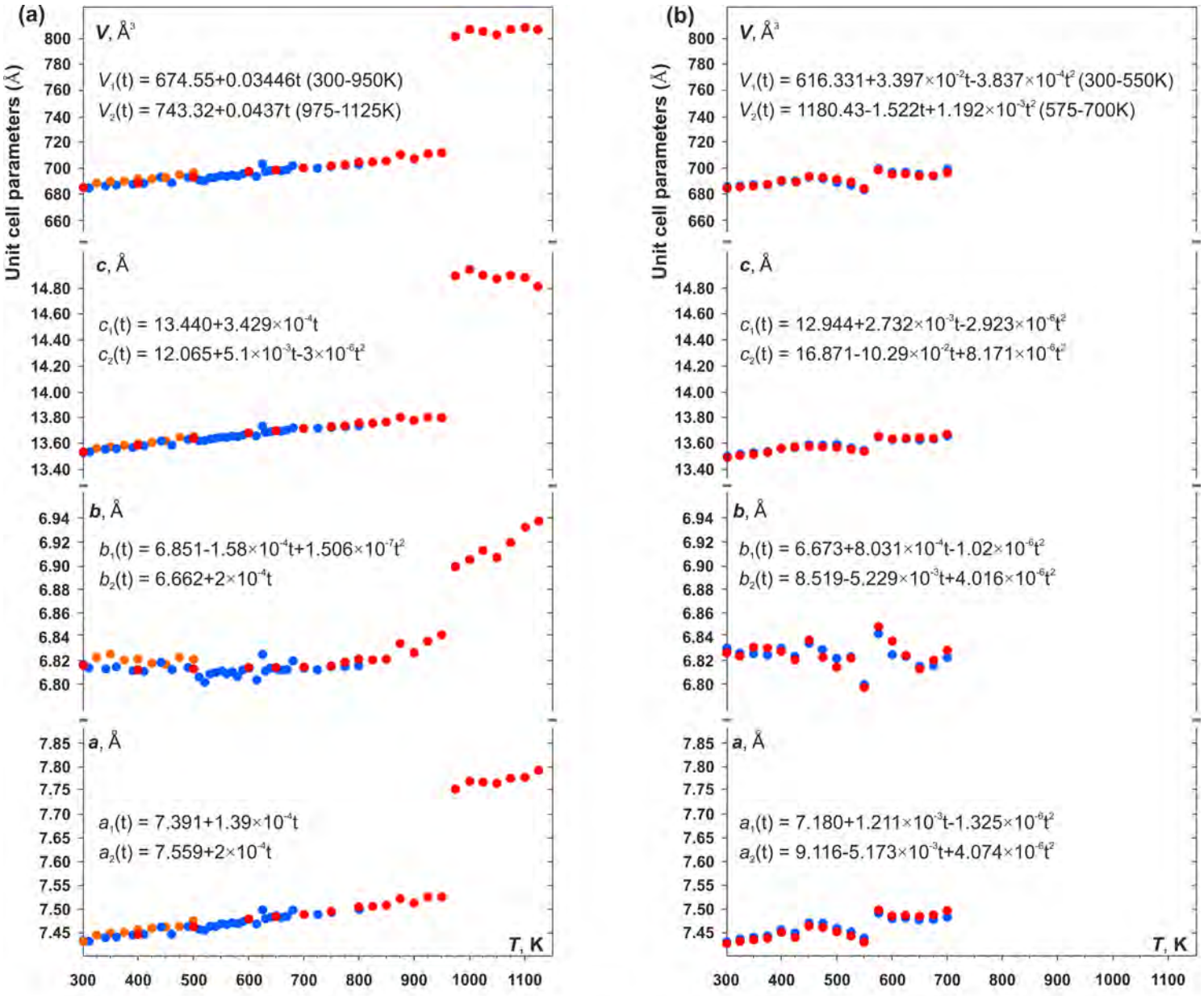

Figure 5

This is the peer-reviewed, final accepted version for American Mineralogist, published by the Mineralogical Society of America.
The published version is subject to change. Cite as Authors (Year) Title. American Mineralogist, in press.
DOI: https://doi.org/10.2138/am-2022-8753. http://www.minsocam.org/

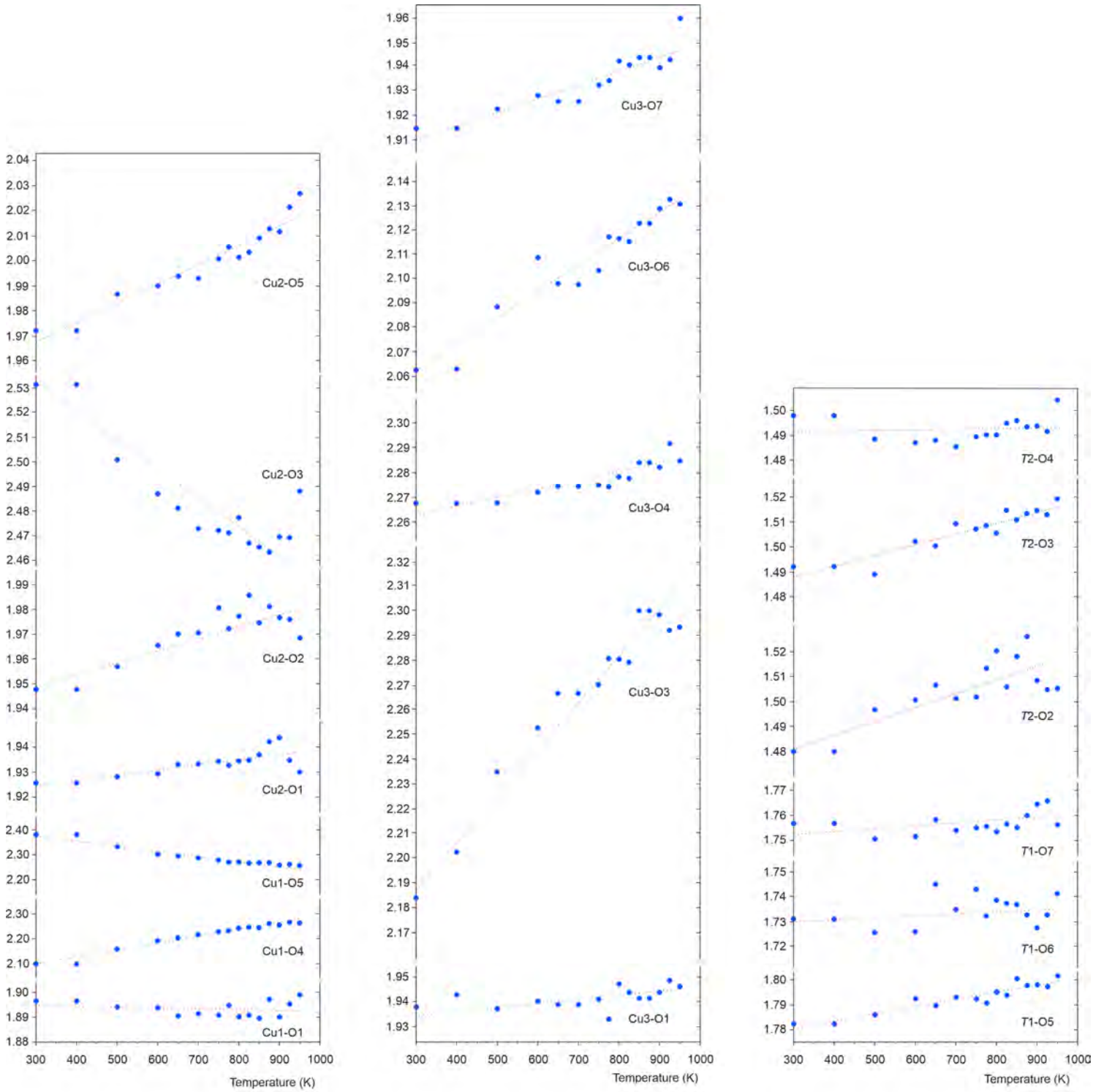

Figure 6

This is the peer-reviewed, final accepted version for American Mineralogist, published by the Mineralogical Society of America.
The published version is subject to change. Cite as Authors (Year) Title. American Mineralogist, in press.
DOI: https://doi.org/10.2138/am-2022-8753. http://www.minsocam.org/

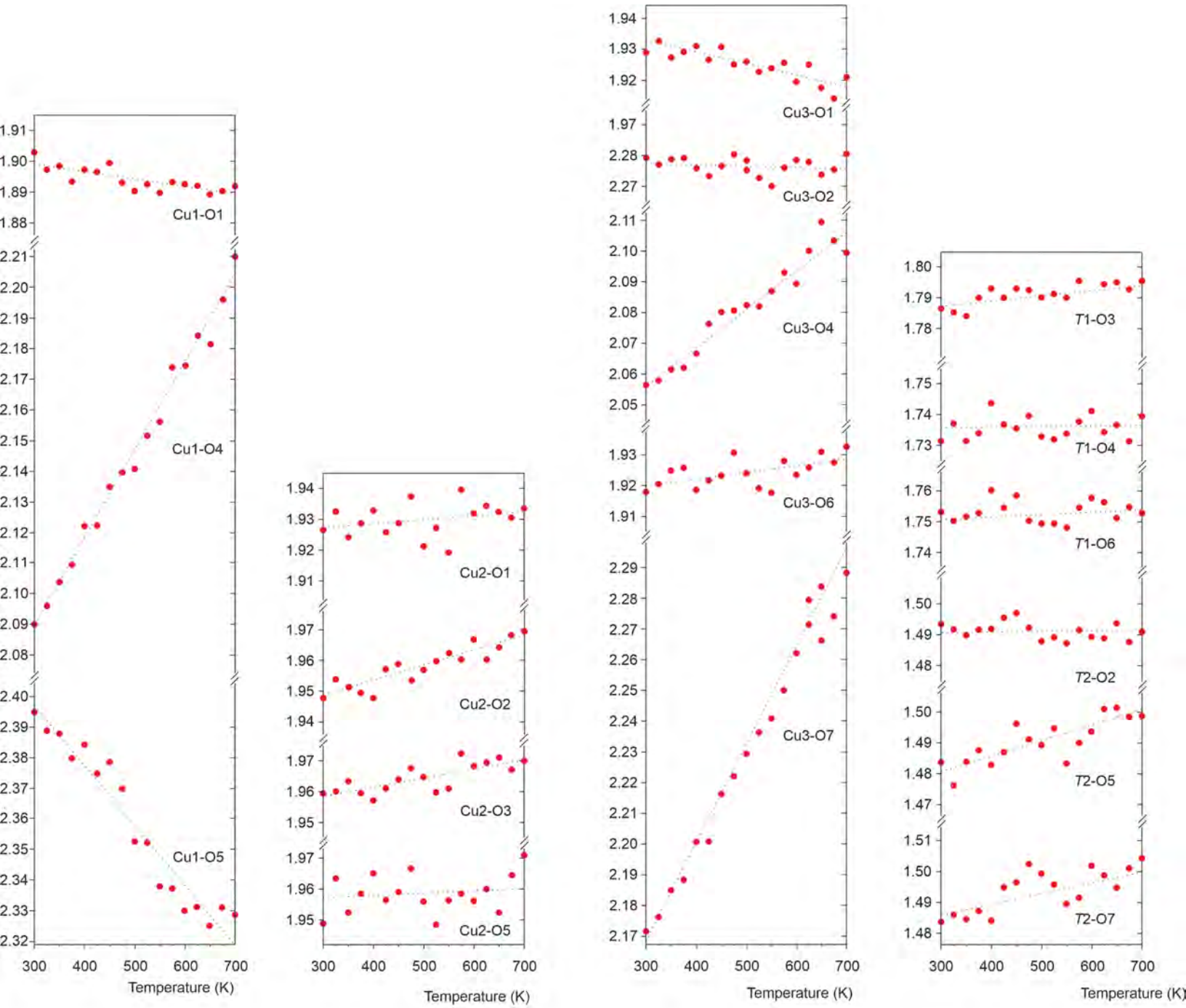

Figure 7

This is the peer-reviewed, final accepted version for American Mineralogist, published by the Mineralogical Society of America.
The published version is subject to change. Cite as Authors (Year) Title. American Mineralogist, in press.
DOI: https://doi.org/10.2138/am-2022-8753. http://www.minsocam.org/

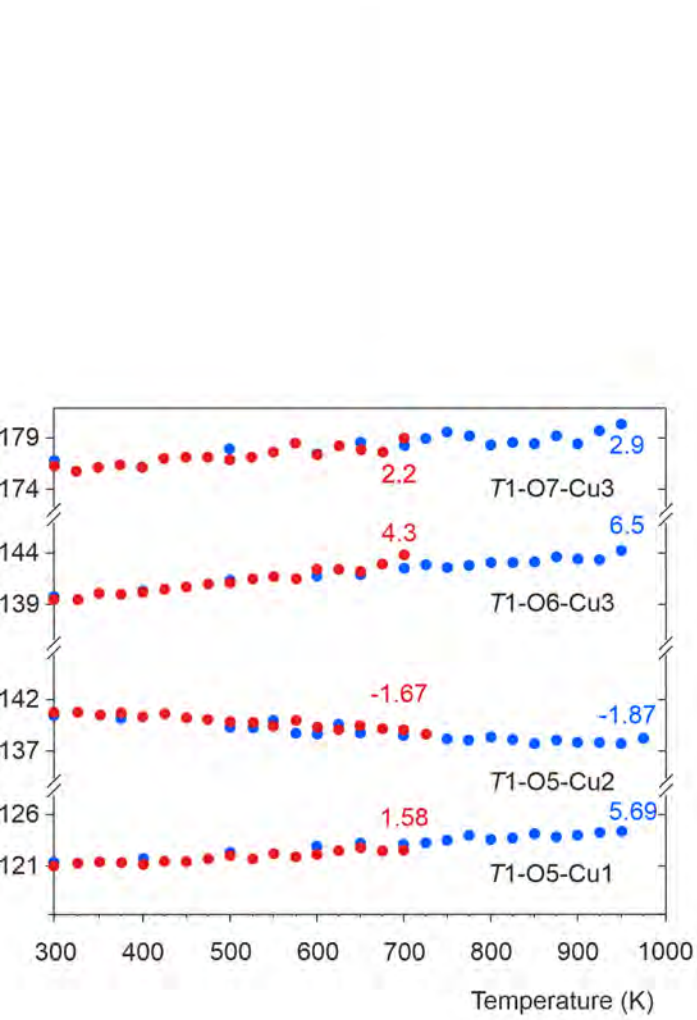

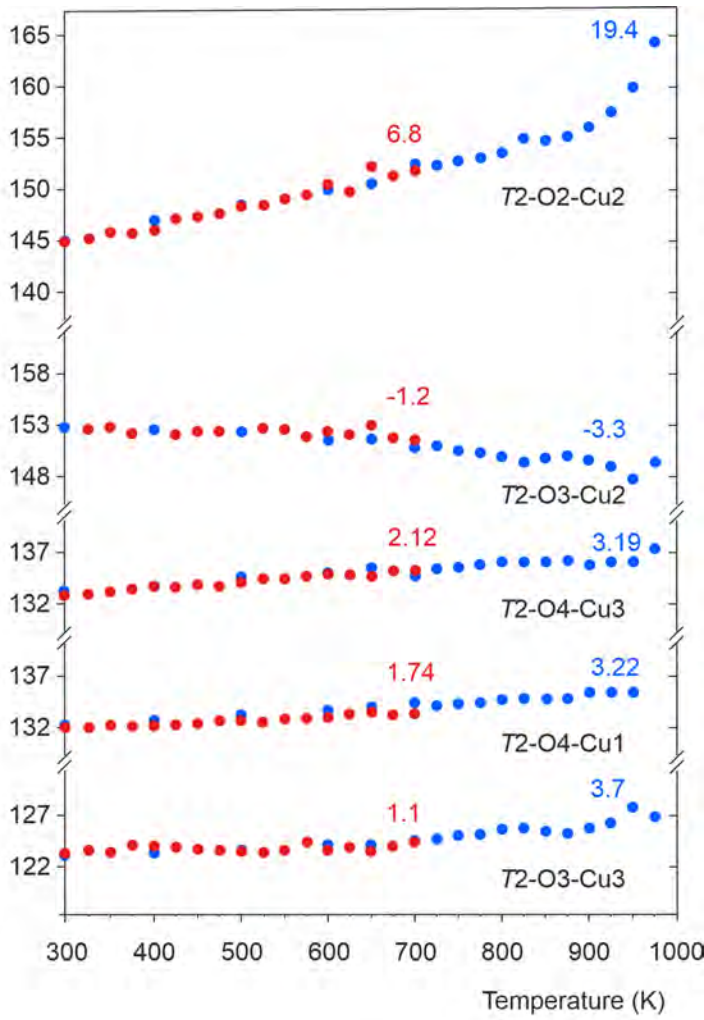

Figure 8